INDIAN INSTITUTE OF TECHNOLOGY GANDHINAGAR

Project - III

Subject: ES-607- Foundations of Fluid Dynamics

Name of Student:
Mayank Awasthi (24250054)
Sivam Behera(24250091)
Sohan Kumar Pradhan (24250091)

Branch: Mechanical Engineering

Submission Date: 24th November 2024

Contents

1 Problem Statement

Consider a flow of an incompressible, viscous fluid (density ρ, viscosity μ) around a sphere of radius a placed in a uniform stream U. The fluid will exert a drag force on the sphere, which is denoted as, say F_D. The drag coefficient, defined as the drag force nondimensionalized by $\rho U^2/2$ and the projected area πa^2, is

$$C_D = \frac{F_D}{(\rho U^2 \pi a^2/2)}.$$

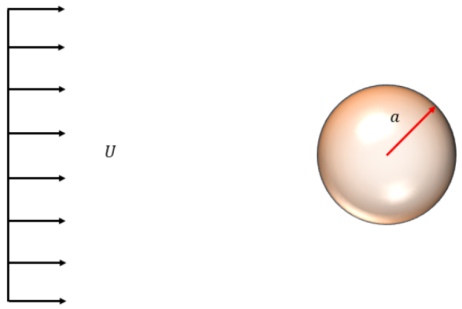

Figure 1: Uniform flow past a sphere

Simulate the flow around the sphere using computational fluid dynamics (CFD) software such as ANSYS, COMSOL, or OpenFOAM (your choice). Plot the variation of drag coefficient (C_D) as a function of the Reynolds number (Re) in the range of $Re = 0.01 - 100$. Clearly indicate how to compute the drag force from the results of the velocity and pressure field $(\mathbf{v}, p)$ that the CFD package will give as output.

For small values of the Reynolds number ($Re \ll 1$), the drag force may be found analytically and has the expression:

$$F_D = F_{D,s}\left\{1 + \frac{3}{8}Re + \frac{9}{40}Re^2\left(\log Re + \gamma + \frac{5}{3}\log 2 - \frac{323}{360}\right) + \frac{27}{80}Re^3 \log Re + O(Re^3)\right\},$$

where $F_{D,s} = 6\pi\mu Ua$ is the Stokes' drag and $\gamma = 0.57721$ is Euler's constant. Compare the simulated results for C_D with the above analytical result (after writing it in terms of C_D instead of F_D). In your final report, you have to clearly outline the equations, boundary conditions,the domain chosen for the numerical simulation, mesh size and type, along with mesh-independence test.

2 The Governing Equations to be solved

The problem specifically requires varying the Reynolds number (Re) to obtain the drag coefficient (C_D) for flow past a sphere. To achieve a generalized solution, the analysis is conducted using a dimensionless framework, which provides several significant advantages, such as enabling comprehensive parametric studies, reduced computational complexity, and systematic variation of the Reynolds number (Re). By nondimensionalizing the governing equations, we remove the dependence on specific fluid properties, such as density (ρ) and viscosity (μ), and instead focus on the universal behavior of fluid flow characterized by Re. This approach ensures the results are versatile and can be applied to a wide range of flow regimes and conditions.

The governing equations used in this study are as follows: Simplified Navier-Stokes equation, along with continuity for incompressible, viscous fluid flow are:

$$\rho\left[(\mathbf{v}\cdot\nabla)\mathbf{v}\right] = -\nabla p + \mu\nabla^2\mathbf{v}, \quad \text{and} \quad \rho\nabla\cdot\mathbf{v} = 0,$$

where $\mathbf{v}$ is the velocity field, p is the pressure, ρ is the fluid density, and μ is the dynamic viscosity.

Through nondimensionalization, using characteristic scales such as velocity U, length a (sphere radius), and dynamic pressure ρU^2, the equations transform into their nondimensional form:

$$\mathrm{Re}\left[(\mathbf{v}^* \cdot \nabla^*)\mathbf{v}^*\right] = -\nabla^* p^* + \nabla^{*2}\mathbf{v}^*, \quad \nabla^* \cdot \mathbf{v}^* = 0$$

where $Re = \frac{\rho U a}{\mu}$ is the Reynolds number. Here, the velocity, pressure, and spatial derivatives are now dimensionless quantities ($\mathbf{v}^*$, p^*, ∇^*).

Physical Interpretation: By transforming the equations, the role of Re becomes clear. The inertial term having density (ρ) on the left-hand side scales to Re, reflecting its role in determining inertial forces, whereas the viscosity (μ) on the right-hand side turns unity, representing the relative contribution of viscous forces.

This nondimensionalized form is implemented in *COMSOL Multiphysics* using its PDE module, where nondimensional parameters such as Re can be systematically varied. This allows for efficient parametric sweeps of Re and enables the extraction of flow variables, such as velocity and pressure, to compute the drag force and drag coefficient.

3 Assumptions

To simplify the analysis and focus on the primary flow behavior, several assumptions are made during the formulation and implementation of the governing equations:

- **Incompressible Flow:** The fluid density (ρ) is assumed to be constant, implying that compressibility effects are negligible. This is a valid assumption for flows with low Mach numbers, typically much less than 0.3.
- **Steady-State Conditions:** The flow is considered to have reached a steady state, where transient effects are absent, and all time derivatives ($\partial/\partial t$) in the Navier-Stokes equations are zero.
- **Newtonian Fluid:** The fluid exhibits a linear relationship between stress and strain rate, characterized by a constant dynamic viscosity (μ). Non-Newtonian effects, such as shear-thinning or thickening, are ignored.
- **Laminar Flow Regime:** The Reynolds number (Re) is within the range where flow remains laminar. This is critical for validating analytical comparisons and ensures that turbulence models are not required.
- **Negligible Body Forces:** External body forces, such as gravitational or electromagnetic forces, are considered negligible compared to inertial and viscous forces acting on the fluid.
- **Uniform Far-Field Velocity:** The velocity far from the sphere is uniform and parallel to the main axis of interest. This simplifies boundary conditions and reflects idealized external flow conditions.
- **Axisymmetric Flow:** The flow field is assumed to be symmetric about the axis passing through the center of the sphere. This reduces computational complexity by eliminating azimuthal variations in the solution.
- **No-Slip Boundary Condition:** The fluid velocity at the sphere's surface is assumed to be zero relative to the surface, ensuring accurate representation of viscous effects at the boundary.

4 Numerical Scheme for Simulating Flow Past a Sphere in COMSOL

In computational fluid dynamics (CFD) using COMSOL, the numerical scheme involves several critical methods designed to approximate the solutions of partial differential equations (PDEs) governing fluid flow. This section explains the finite element method (FEM), linear and nonlinear solvers, stabilization techniques, and time-stepping algorithms in detail, focusing on the techniques used in COMSOL.

4.1 Finite Element Method (FEM)

4.1.1 Discretization

The Navier-Stokes equations are discretized using FEM. The computational domain is divided into smaller finite elements, and the solution is approximated within each element using linear Lagrange shape functions (P1 elements) for both velocity and pressure fields.

The velocity field $\mathbf{u}(x)$ and pressure field $p(x)$ are expressed as:

$$\mathbf{u}(x) = \sum_{i=1}^{N} \phi_i(x)\mathbf{u}_i, \quad p(x) = \sum_{j=1}^{M} \psi_j(x)p_j$$

where:

- ϕ_i and ψ_j: shape functions
- $\mathbf{u}_i$, p_j: nodal values of velocity and pressure
- N, M: number of nodes in an element

4.1.2 Weak Formulation

The PDEs are converted into their weak form by multiplying with test functions $\mathbf{v}$ and integrating over the domain:

$$\int_\Omega \mathbf{v} \cdot \rho(\mathbf{u} \cdot \nabla \mathbf{u})\, d\Omega + \int_\Omega \mathbf{v} \cdot \nabla p\, d\Omega - \int_\Omega \mathbf{v} \cdot \mu \nabla^2 \mathbf{u}\, d\Omega = \int_\Omega \mathbf{v} \cdot \mathbf{F}\, d\Omega$$

Similarly, the continuity equation becomes:

$$\int_\Omega q\, \nabla \cdot \mathbf{u}\, d\Omega = 0$$

where q is the test function for pressure.

The weak formulation ensures the equations are satisfied in an average sense, enabling FEM to handle complex geometries and boundary conditions.

4.2 Mesh Configuration

The computational domain is meshed using 2D triangular elements. The mesh is calibrated for fluid dynamics with the following features:

- **Refinement Near Boundaries:** Extremely fine mesh near the sphere to resolve the boundary layer.
- **Boundary Layer Elements:** Specialized elements with anisotropic stretching to accurately capture velocity gradients.

Mesh quality significantly impacts the accuracy of the simulation. A finer mesh ensures accurate resolution of flow details, especially in regions of high gradients such as wakes and vortices.

4.3 Solver Techniques

4.3.1 Stationary Solver

For steady-state problems, COMSOL employs a continuation method:

- The equations are solved iteratively by gradually increasing the applied boundary conditions (e.g., inlet velocity) from a small initial value.
- This helps the nonlinear solver converge to the correct solution.

4.3.2 Nonlinear Solver: Newton-Raphson Method

The nonlinear system of equations resulting from the discretized Navier-Stokes equations is solved using the Newton-Raphson iterative method with an adaptive damping strategy. The problem is formulated as $\mathbf{F}(\mathbf{u}) = \mathbf{0}$, where $\mathbf{F}$ is the nonlinear operator, and $\mathbf{u}$ is the solution vector containing velocity and pressure unknowns. The damped Newton method is outlined as follows:

For iteration $k = 0, 1, 2, \ldots$:

1. Solve the linearized system:
$$\mathbf{J}(\mathbf{u}^k)\delta\mathbf{u}^k = -\mathbf{F}(\mathbf{u}^k),$$
where $\mathbf{J}(\mathbf{u}^k) = \frac{\partial \mathbf{F}}{\partial \mathbf{u}}\big|_{\mathbf{u}^k}$ is the Jacobian matrix evaluated at the current iteration, and $\delta\mathbf{u}^k$ is the correction vector.
2. Update the solution:
$$\mathbf{u}^{k+1} = \mathbf{u}^k + \lambda_k \delta\mathbf{u}^k,$$
where $\lambda_k \in (0, 1]$ is the damping parameter.

The damping parameter λ_k is adaptively chosen to ensure global convergence. A typical strategy involves:

$$\lambda_k = \min\left(1, \frac{\|\mathbf{F}(\mathbf{u}^k)\|_2}{\|\mathbf{J}(\mathbf{u}^k)\delta\mathbf{u}^k\|_2}\right).$$

The Jacobian matrix $\mathbf{J}(\mathbf{u}^k)$ incorporates the linearization of the nonlinear convective terms. Specifically, the Jacobian contribution from the convective term $(\mathbf{u} \cdot \nabla)\mathbf{u}$ is given as:

$$\mathbf{J}(\mathbf{u}^k)\delta\mathbf{u} = (\mathbf{u}^k \cdot \nabla)\delta\mathbf{u} + (\delta\mathbf{u} \cdot \nabla)\mathbf{u}^k.$$

This accounts for the coupling between velocity components introduced by the convective acceleration.

For highly nonlinear flow regimes, a modified convergence criterion is employed to ensure stability and accuracy:

$$\|\mathbf{F}(\mathbf{u}^k)\|_2 < \epsilon_{\text{tol}} \|\mathbf{F}(\mathbf{u}^0)\|_2,$$

where ϵ_{tol} is a user-defined tolerance, typically set to 10^{-6}. This relative convergence criterion ensures the solution's accuracy while avoiding premature termination of the iterations.

The damped Newton-Raphson method demonstrates quadratic convergence near the solution and is robust for complex flow configurations. The analytical Jacobian, combined with the adaptive damping strategy, typically reduces the residual norm within 5 to 10 iterations for well-posed problems.

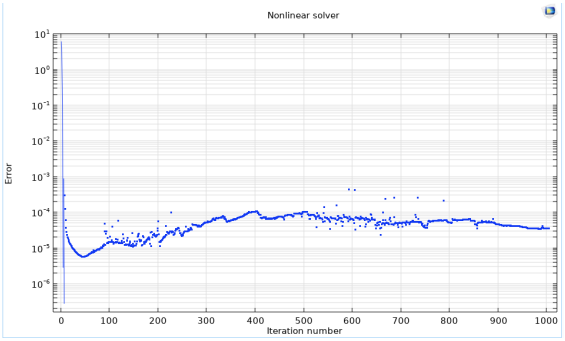

Figure 2: Non Linear Solver Graph

4.3.3 Linear System Solvers

PARDISO Direct Solver: Pardiso Solver employs a direct approach for solving $\mathbf{Ax} = \mathbf{b}$ using LU decomposition. For symmetric positive definite matrices, the factorization is:

$$\mathbf{A} = \mathbf{PLDL}^\top \mathbf{P}^\top,$$

where $\mathbf{P}$ is a permutation matrix, $\mathbf{L}$ is a lower triangular matrix, and $\mathbf{D}$ is a diagonal or block-diagonal matrix. For unsymmetric matrices, the decomposition takes the form:

$$\mathbf{PAQ} = \mathbf{LU},$$

where $\mathbf{P}$ and $\mathbf{Q}$ are row and column permutation matrices, $\mathbf{L}$ is unit lower triangular, and $\mathbf{U}$ is upper triangular. The solution process involves:

- Symbolic Factorization: Determines the sparsity pattern for $\mathbf{L}$ and $\mathbf{U}$.
- Numerical Factorization: Computes the LU decomposition.
- Forward and Backward Substitution: Solves $\mathbf{Ly} = \mathbf{Pb}$ and $\mathbf{Ux} = \mathbf{y}$.

$$\mathbf{Ly} = \mathbf{Pb}, \quad \mathbf{Ux} = \mathbf{y}.$$

PARDISO is optimized for shared-memory parallel architectures, making it well-suited for large systems with up to 10^6 degrees of freedom. It employs advanced reordering algorithms to minimize fill-in and ensures numerical stability using pivot perturbation techniques. For systems exceeding memory constraints, GMRES becomes the preferred solver due to its iterative nature and lower memory requirements.

GMRES Method: The linearized system $\mathbf{Ax} = \mathbf{b}$ obtained at each Newton-Raphson iteration can also be solved using the Generalized Minimal Residual (GMRES) method. GMRES is an iterative Krylov subspace method designed to minimize the residual norm:

$$\min \|\mathbf{b} - \mathbf{Ax}\|_2, \quad \mathbf{x} \in \mathbf{x}_0 + \mathcal{K}_m,$$

where $\mathcal{K}_m = \text{span}\{\mathbf{r}_0, \mathbf{Ar}_0, \mathbf{A}^2\mathbf{r}_0, \ldots, \mathbf{A}^{m-1}\mathbf{r}_0\}$ is the Krylov subspace generated from the initial residual $\mathbf{r}_0 = \mathbf{b} - \mathbf{Ax}_0$.

The algorithm proceeds as follows:

1. Perform the Arnoldi iteration to generate an orthonormal basis $\{\mathbf{v}_1, \ldots, \mathbf{v}_m\}$ of the Krylov subspace $\mathcal{K}_m$. This process constructs the upper Hessenberg matrix $\mathbf{H}_m \in R^{m \times m}$ such that:

   $$\mathbf{AV}_m = \mathbf{V}_m \mathbf{H}_m + h_{m+1,m} \mathbf{v}_{m+1} \mathbf{e}_m^T,$$

   where $\mathbf{V}_m$ is the matrix with columns $\{\mathbf{v}_1, \ldots, \mathbf{v}_m\}$, and $h_{m+1,m}$ represents the last entry in the decomposition.

2. Solve the least-squares problem:

   $$\min \|\beta \mathbf{e}_1 - \mathbf{H}_m \mathbf{y}\|_2,$$

   where $\beta = \|\mathbf{r}_0\|_2$ and $\mathbf{e}_1 = [1, 0, \ldots, 0]^T \in R^m$.

3. Update the solution as:

   $$\mathbf{x} = \mathbf{x}_0 + \mathbf{V}_m \mathbf{y}.$$

The orthonormal basis $\mathbf{V}_m$ ensures numerical stability, while the residual minimization guarantees rapid convergence for well-conditioned systems. GMRES is particularly effective for solving sparse, nonsymmetric systems, such as those arising in the linearized Navier-Stokes equations.

The method's performance depends on the spectral properties of $\mathbf{A}$. For ill-conditioned systems, preconditioning techniques are often applied to transform the problem into $(\mathbf{M}^{-1}\mathbf{A})\mathbf{x} = \mathbf{M}^{-1}\mathbf{b}$, where $\mathbf{M}$ is a preconditioner that improves convergence.

4.4 Stabilization Techniques

To prevent numerical instabilities, especially in convection-dominated flows, the following stabilization methods are employed:

- **Streamline Upwind Petrov-Galerkin (SUPG):** Adds artificial diffusion along streamlines:
$$\mathbf{R}^{\text{SUPG}} = \mathbf{R} + \tau(\mathbf{u} \cdot \nabla \mathbf{u}) \cdot \nabla \phi$$
where τ is a stabilization parameter.
- **Pressure Stabilization Petrov-Galerkin (PSPG):** Stabilizes pressure by adding terms proportional to residuals of the continuity equation.
- **Crosswind Diffusion:** Diffuses gradients perpendicular to streamlines, ensuring stability near sharp features.

4.5 Time-Stepping Methods

For transient problems, COMSOL uses the Backward Differentiation Formula (BDF):

$$\frac{\partial \mathbf{u}}{\partial t} \approx \sum_{i=0}^{k} \alpha_i \mathbf{u}^{n-i}$$

where k is the order of the method (typically $k = 2$).

This implicit scheme:

- Is unconditionally stable for stiff systems.
- Allows large time steps compared to explicit methods.

5 Numerical Methodology and Implementation Details

5.1 Introduction to the Simulation Approach

For simulating a 3D laminar flow problem, we utilized the 2D axisymmetric physics option in COMSOL Multiphysics. This choice significantly reduces computational cost and effort while maintaining accuracy, particularly in symmetric configurations like ours. The axisymmetric assumption is advantageous when the problem geometry and boundary conditions exhibit rotational symmetry around an axis.

5.2 Physics Setup

5.2.1 Physics Interface and Model Settings

- The **Single-Phase Flow** interface under Fluid Flow was chosen to model the system due to its capability to handle low Mach number flows ($Ma < 0.3$).
- The **Laminar Flow** model was applied because the problem was constrained to a Reynolds number range of $0.1 \leq Re \leq 100$, far below the $Re = 2000$ threshold for turbulence in classical pipe flow.
- A **stationary study** (time-independent analysis) was employed, considering that transient effects were not critical for this study.

5.3 Geometry Setup

5.3.1 Axisymmetric Configuration

The geometry was constructed in 2D and revolved about the axial (z) direction about $r = 0$ to form a 3D axisymmetric representation.

5.3.2 Building Components

1. **Sphere Representation:** A circle with a radius of 1, centered at $(0, 0)$, was provided a sector angle of 180° (with a $-90°$ offset) to form a sphere when revolved about the z-direction.
2. **Outer Rectangle:** Defined with width $W = 70$ and height $H = 50$, positioned at $r = 0, z = -H/2$. It forms a cylindrical domain enclosing the sphere. The extensive domain dimensions were specifically chosen to minimize wall effects and ensure fully developed flow conditions, critical for accurate drag coefficient computation.
3. **Inner Rectangle:** A smaller rectangle with width 5 and height H was added to use as a mesh control edge to refine the mesh near the sphere.

Insights

- **Outer Boundary Size:** Increasing the size of the outer rectangle (in 2D) or cylinder (in 3D) minimizes the influence of boundary effects, ensuring a more realistic simulation.
- **Inner Region Refinement:** A smaller cylindrical domain near the sphere allows finer meshing for improved accuracy in regions with steep gradients.

5.4 Material Properties

For non-dimensional analysis, we avoid choosing any specific material for the fluid. Instead, to conduct a generalized study of the Reynolds number, we selected the following properties:

- Density (ρ) = Reynolds number (Re)
- Dynamic viscosity (μ) = 1

5.5 Domain Selection

The primary computational domain consists of the region where fluid flow occurs. In this case, the outer rectangular region without the sphere was selected as the fluid domain. The choice of this domain allows the solver to apply the Navier-Stokes equations only to the regions where the fluid exists, avoiding unnecessary computation in the sphere's regions obstructing the flow.

5.6 Boundary Conditions

Axial Symmetry The axial symmetry condition was enforced along $r = 0$, excluding the sphere.

No-Slip Walls The sphere's surface and the outer walls of the rectangular domain were assigned no-slip conditions.

Inlet and Outlet

1. **Inlet:** A velocity inlet condition was applied to the front face of the outer rectangle, with $u_r = 0, u_\phi = 0, u_z = 1$, ensuring a uniform flow in the axial direction.
2. **Outlet:** A zero-pressure outlet boundary condition was applied at the back face of the rectangle. Backflow was suppressed to stabilize the solution.

5.7 Mesh Design

5.7.1 Mesh Setup

A user-controlled meshing strategy was adopted:

- The **outer domain** was meshed using a "Finer" predefined setting:
  - Maximum element size: 1.4
  - Minimum element size: 0.02
  - Curvature factor: 2.5
- The **inner domain** near the sphere used "Extremely Fine" meshing:
  - Maximum element size: 0.335
  - Minimum element size: 0.001
  - Curvature factor: 2.0

5.7.2 Meshing Methodology

A free triangular mesh was applied in 2D, which automatically tessellates upon revolution to form a 3D axisymmetric mesh. The number of iterations was set to 4 for enhanced meshing near the sphere.

Insights

- **Mesh Size vs. Computational Time:** Finer meshes increase the number of elements, leading to higher computational time due to solving larger linear systems.
- **Mesh Size vs. Accuracy:** Smaller mesh sizes improve solution accuracy but beyond a critical refinement, additional improvements are negligible, emphasizing the need for mesh independence studies.

5.8 Solver Configuration

5.8.1 Stationary Solver

The stationary solver was configured with:

- $P1 + P1$ discretization for pressure and velocity fields.
- An auxiliary sweep to evaluate flow behavior for $0.1 \leq Re \leq 100$.

5.8.2 Computational Details

- The computation involved solving approximately 33,000 degrees of freedom.
- **PARDISO direct solver** was employed to ensure robustness and efficiency.

6 Study and Analysis

6.1 Velocity Profiles

- **Velocity Magnitude Analysis (`spf.U`):** At lower Reynolds numbers (Re=0.5), the flow exhibited creeping behavior with minimal inertial effects, dominated by viscous forces. As Re increased e.g.-20, inertial forces created streamlined yet stronger axial flows.
- **Components Analysis (u, v, w):** When substituting u, v, w instead of `spf.U` in the expression, the resulting plots revealed the following:

– The radial velocity (u) decreased significantly with an increase in inertial forces, showing the suppression of radial flow.

– Azimuthal flow was negligible due to the symmetric geometry.

– Axial flow dominated the dynamics.

6.2 Boundary layer

From the velocity profile, boundary layer formation is evident. At low Reynolds numbers (creeping flow), the boundary layer is diffuse, with flow smoothly wrapping around the sphere, showing negligible inertial effects. In contrast, at high Reynolds numbers, a thinner boundary layer develops, accompanied by flow separation and wake formation due to dominant inertial forces, highlighting stark differences in flow behavior.

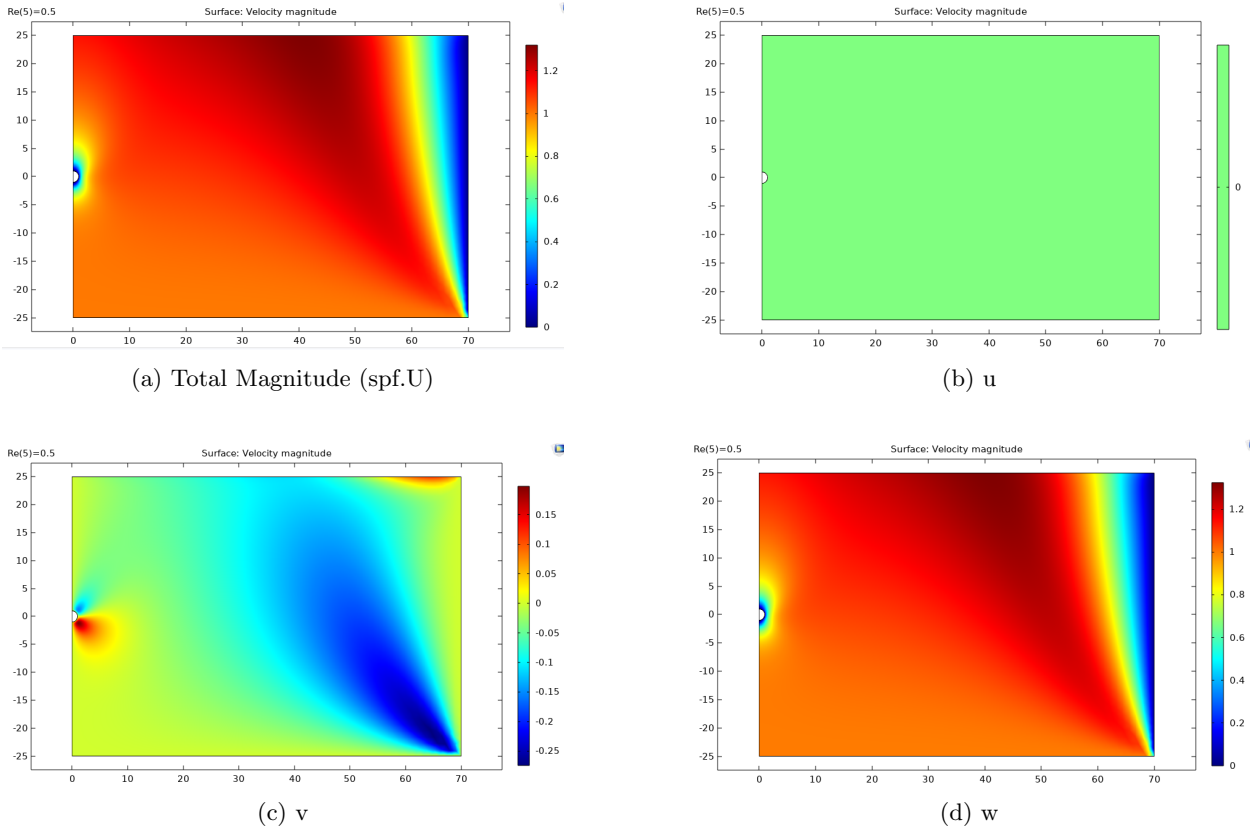

(a) Total Magnitude (spf.U)

(b) u

(c) v

(d) w

Figure 3: Velocity components at Re=0.5

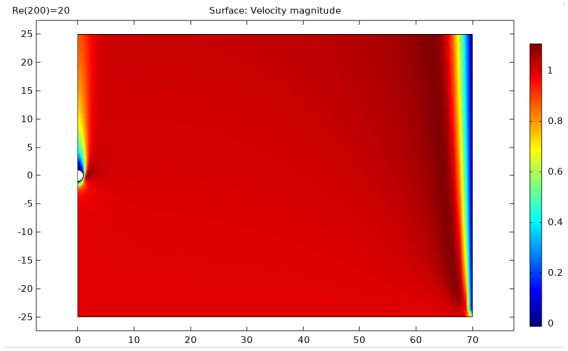

(a) Total Magnitude (spf.U)

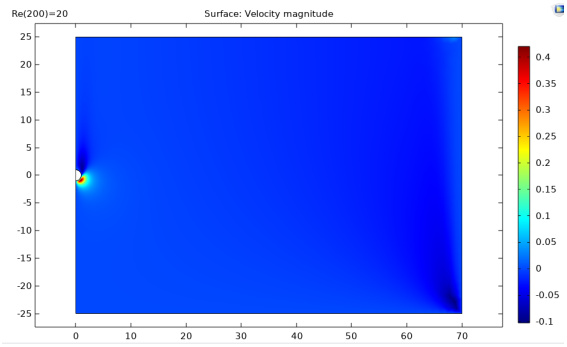

(b) u

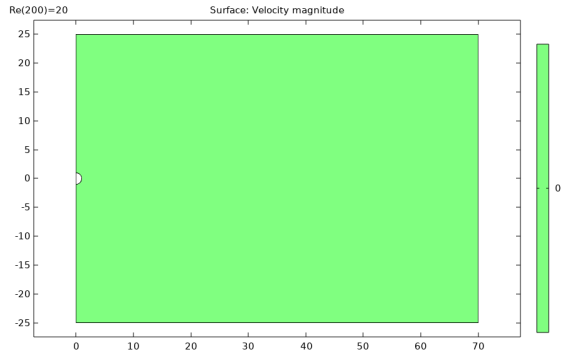

(c) v

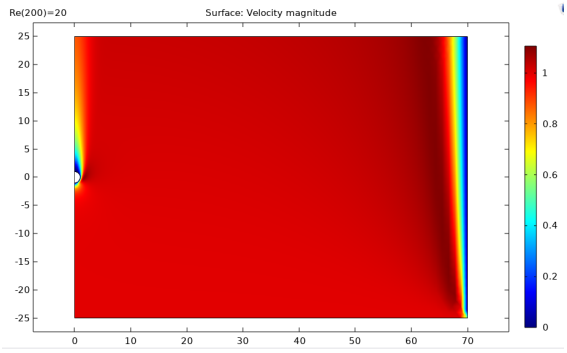

(d) w

Figure 4: Velocity components at Re=20

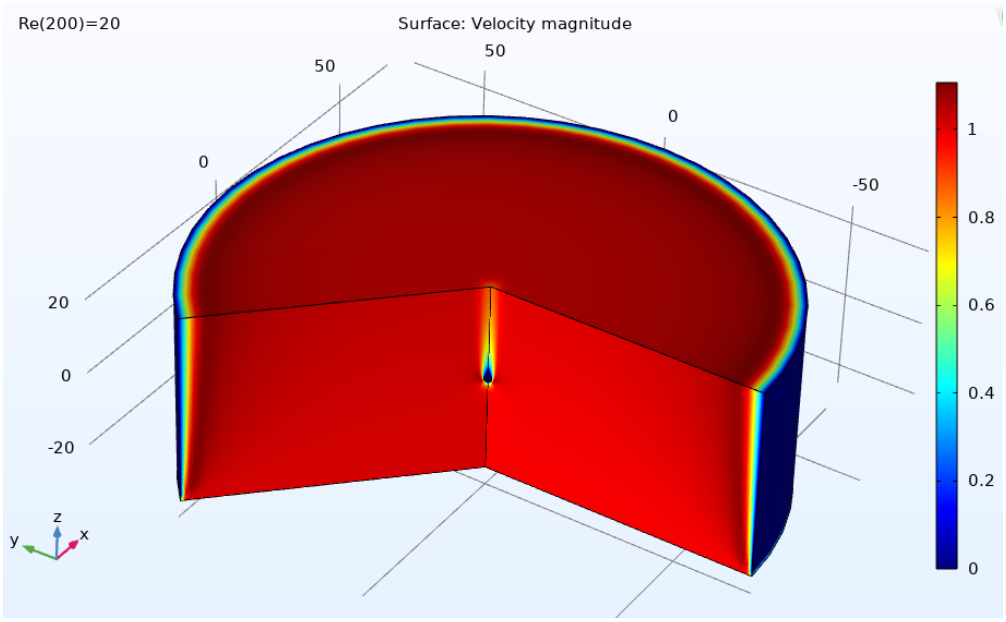

Figure 5: 3D Flow visualization around the sphere

6.3 Pressure Distribution

At low Reynolds numbers ($Re = 0.5$), the flow exhibits creeping behavior, with high pressure on the sphere's front due to stagnation and a smooth decline along the surface, resulting in negligible wake formation. At higher Reynolds numbers ($Re = 20$), inertial effects become significant, leading to flow separation and a distinct wake region behind the sphere, causing an asymmetric pressure distribution with lower rear pressure.

The red region at the boundary represents localized high pressure, likely caused by the interaction of the incoming flow with the domain boundary. This could arise from boundary condition constraints or recirculation effects near the corner, emphasizing the need for careful domain and mesh calibration to minimize numerical artifacts.

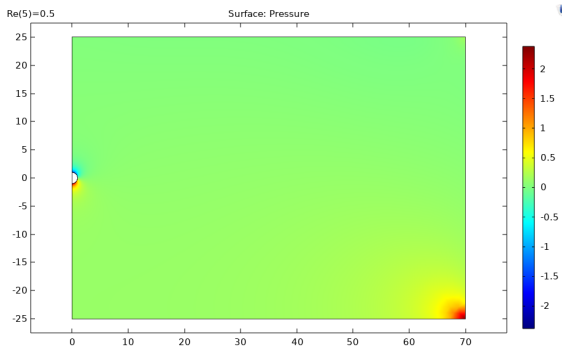

(a) for Re = 5

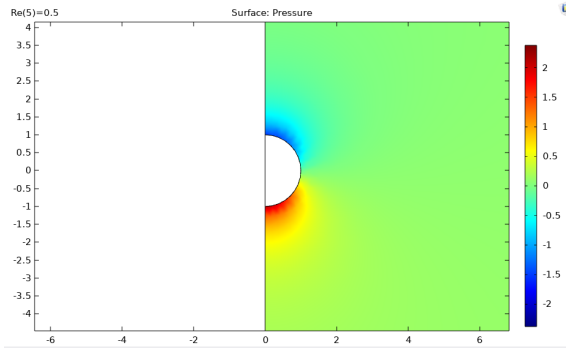

(b) for Re = 5

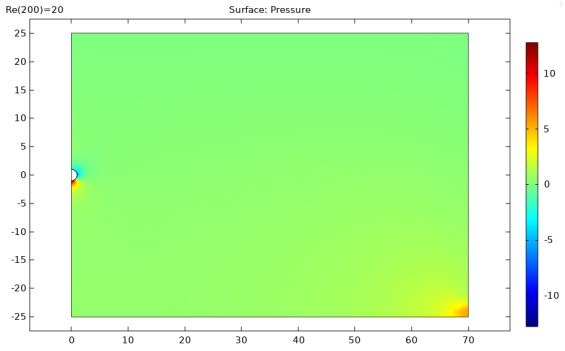

(c) for Re = 20

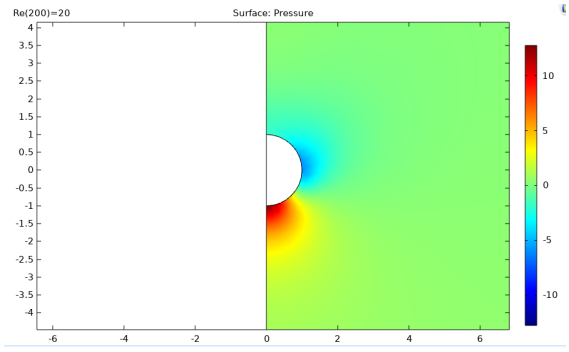

(d) for Re = 20

Figure 6: Pressure Distribution around Sphere

7 User Instructions for Reproducing Study Results

To conduct accurate simulations of flow past a sphere using COMSOL Multiphysics, this section provides essential guidelines for non-dimensional and dimensional studies, including parameter adjustments, domain settings, and mesh refinement.

7.1 Non-Dimensional Study

- **Reynolds Number (Re):** Parameterize Re globally using the relation:

$$\mathrm{Re} = \frac{\rho U_\infty D}{\mu}$$

  where ρ, U_∞, D, and μ are fluid density, free-stream velocity, sphere diameter, and dynamic viscosity, respectively. Changing Re directly modifies flow behavior and resultant forces.

- **Mesh Refinement:** Employ a finer mesh near the sphere surface to resolve boundary layers and transitions to coarser elements in the far field to balance accuracy and computational cost. Excessively dense meshes increase precision but also computational load.

- **Domain Dimensions (Axisymmetric):** Adjust the rectangular domain height (H) and width (W) to minimize boundary effects while maintaining computational efficiency:
  - Larger domains improve free-stream representation but increase computational demands.
  - Insufficient domain size can distort flow fields near boundaries.

7.2 Dimensional Study

- **Physical Parameters:** Explicitly define key variables like μ, U_∞, R, and ρ for dimensional analysis. Adjust these to simulate specific flow regimes:
  - Decreasing U_∞ or increasing μ captures low Re flows (e.g., creeping flow).
  - Increasing R necessitates proportional domain enlargement to avoid confinement effects.

7.3 Practical Insights

- **Mesh and Domain Sensitivity:** Refined meshes reduce numerical diffusion and improve gradient accuracy, while excessively coarse meshes may underresolve key flow features. Larger domains reduce boundary-induced artifacts but increase solver time.

- **Solver Settings:** Use steady solvers for low Re flows; for unsteady conditions (e.g., vortex shedding at high Re), switch to time-dependent solvers. Tight solver tolerances improve convergence, especially for creeping flow.

- **Validation and Scalability:** Validate results against analytical ($C_D = 24/\mathrm{Re}$ for Stokes flow) or experimental data for subcritical Reynolds numbers. Use parametric sweeps to explore effects of Re, mesh density, and domain size systematically.

These instructions ensure efficient setup for both non-dimensional and dimensional studies, leveraging COMSOL's capabilities to achieve accurate and reliable simulation results.

8 Computation of Drag Force from Velocity and Pressure Fields

In fluid flow simulations, the drag force acting on a body, such as a sphere, is determined from the velocity and pressure fields obtained as outputs. The computation begins with the Cauchy stress tensor, which represents the forces per unit area in the fluid, combining contributions from pressure and viscous effects. The stress tensor is expressed as:

$$\boldsymbol{\sigma} = -p\mathbf{I} + \mu\left[\nabla\mathbf{u} + (\nabla\mathbf{u})^T\right] \tag{1}$$

Here, p is the pressure field, $\mathbf{I}$ is the identity tensor, μ is the fluid's dynamic viscosity, and $\nabla\mathbf{u}$ is the velocity gradient tensor. The term $-p\mathbf{I}$ accounts for isotropic pressure forces, while $\mu\left[\nabla\mathbf{u} + (\nabla\mathbf{u})^T\right]$ represents viscous stresses.

The traction vector $\mathbf{t}$, which describes the force per unit area exerted by the fluid on the sphere's surface, is computed as:

$$\mathbf{t} = \boldsymbol{\sigma} \cdot \mathbf{n} \tag{2}$$

where $\mathbf{n}$ is the unit normal vector to the sphere's surface, pointing outward. Expanding $\mathbf{t}$, the equation becomes:

$$\mathbf{t} = \left[-p\mathbf{I} + \mu\left(\nabla\mathbf{u} + (\nabla\mathbf{u})^T\right)\right] \cdot \mathbf{n} \tag{3}$$

This equation incorporates both pressure ($-p\mathbf{n}$) and viscous stresses (terms dependent on μ).

The drag force is obtained by integrating the z-component of $\mathbf{t}$ over the surface of the sphere. For a full 3D surface, this is given by:

$$F_{\text{drag}} = \int_S \mathbf{t} \cdot \mathbf{e}_z \, dS = \int_S \left[-pn_z + \mu\left(\frac{\partial u}{\partial z}n_z + \frac{\partial w}{\partial z}n_r\right)\right] dS \tag{4}$$

where n_z and n_r are components of the surface normal vector in the z- and radial directions, and $\frac{\partial u}{\partial z}, \frac{\partial w}{\partial z}$ are velocity gradients.

In 2D axisymmetric simulations, this computation simplifies. Instead of integrating over the full 3D surface, the integration is performed along the meridional arc of the sphere's profile, scaled by the circumferential contribution due to symmetry. The drag force in this setup is expressed as:

$$F_{\text{drag}} = 2\pi \int_L r\, t_z \, d\ell \tag{5}$$

where r is the radial distance from the axis of symmetry, t_z is the z-component of the traction, and L represents the arc length along the sphere's profile.

In COMSOL, this is automated using the `intop1` operator, and the drag force is computed as:

$$F_{\text{drag}} = 2\pi\, \texttt{intop1}(r \cdot \texttt{spf.T\_stressz}) \tag{6}$$

Here, `spf.T_stressz` represents the z-component of the traction vector extracted from the stress tensor. This method ensures that both pressure and viscous contributions are included.

The drag coefficient C_D is then calculated by normalizing the drag force using the dynamic pressure and reference area:

$$C_D = \frac{F_{\text{drag}}}{\frac{1}{2}\rho U_\infty^2 A} = -\frac{4 \cdot \texttt{intop1}(\texttt{spf.T\_stressz} \cdot r)}{\rho U_\infty^2 \pi R^2} \tag{7}$$

Here, U_∞ is the free-stream velocity, ρ is the fluid density, and $A = \pi R^2$ is the reference area for a sphere of radius R. The factor of 4 arises from the axisymmetric integration and geometric scaling for a full 3D sphere.

The integration is performed over the entire meridional arc (L) of the sphere, where $r = R\sin\phi$ and $d\ell = R\, d\phi$. The process accounts for the axisymmetric formulation, where the surface stress tensor integrates over the arc and scales with $2\pi r$. This approach efficiently captures the drag force without requiring a full 3D mesh, leveraging the symmetry of the flow.

The resultant drag coefficient can be validated against theoretical and empirical results, such as $C_D = \frac{24}{\text{Re}}$ for creeping (Stokes) flow or experimental values for subcritical Reynolds numbers. High-resolution meshing near the stagnation points ensures accurate computation of stress gradients and total drag force. This method highlights the computational efficiency and accuracy achieved by axisymmetric modeling in fluid dynamics simulations.

8.1 Surface Stress Plots

- For low Reynolds numbers ($Re < 1$), the axial surface stress (τ_z) exhibits gradual transitions dominated by viscous effects, with smoother stress variations across the surface. In contrast, at moderate Reynolds numbers ($Re \approx 20$), the stress profile shows pronounced gradients and steeper transitions, especially near the front stagnation point (arc length = 0).

- A key distinction lies in the magnitude of stresses: higher Re cases exhibit significantly larger negative stresses at the stagnation point due to dominant inertial effects. Both regimes display a recovery trend towards the rear of the sphere, but the recovery path and final stress levels differ significantly, reflecting the transition from viscous to inertia-driven flow dynamics.

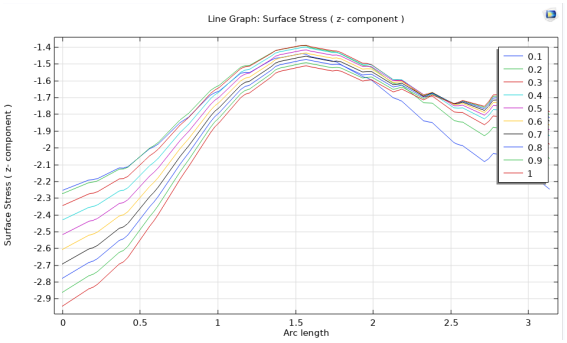

(a) For small Re (0.1-1)

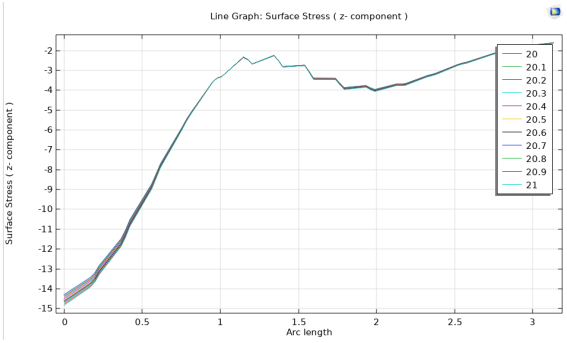

(b) For Re (20-21)

8.2 Drag Force plots

- The drag force variation with Reynolds number reveals distinct trends across flow regimes. In the creeping flow regime ($Re < 1$), the drag force shows subtle non-linear behavior, with a local maximum around $Re \approx 0.3$, highlighting the interplay between dominant viscous forces and weak inertial effects.

- As Re increases, the drag force decreases monotonically, following an approximately logarithmic trend up to $Re \approx 100$. This reflects the transition from viscous-dominated to inertia-influenced flow regimes, aligning with classical sphere drag theory, where drag inversely correlates with Reynolds number prior to the onset of the subcritical drag crisis.

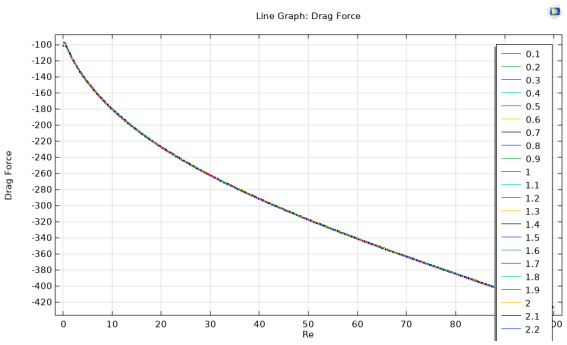

(a) For Re (0.1-100)

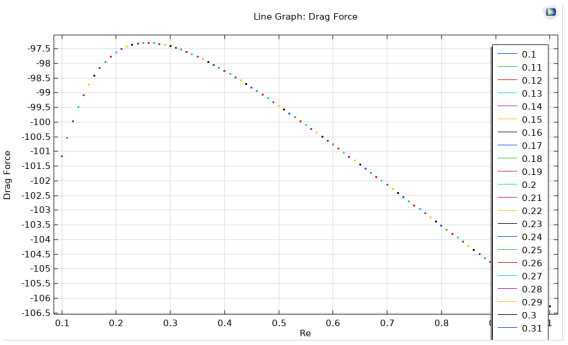

(b) For small Re (0.1-0.3)

9 Drag Coefficient Vs Reynolds number (Re)

- The graph illustrates the relationship between the drag coefficient C_D and the Reynolds number Re for the flow of an incompressible fluid around a sphere. At low Reynolds numbers, the drag coefficient is very high, indicating that the viscous forces dominate over inertial forces in the fluid. This is characteristic of the Stokes flow regime, where the drag coefficient follows the theoretical relation $C_D \propto \frac{24}{Re}$. This steep decline in C_D reflects the strong influence of viscous forces at small Re, where the fluid flows smoothly around the sphere without significant separation or turbulence.

- As Re increases, the drag coefficient decreases less rapidly, transitioning to a regime where both viscous and inertial forces are important. This marks the departure from purely viscous-dominated flow to a more complex interplay between inertia and viscosity. In this intermediate range, the flow becomes less streamlined, and inertial effects start to influence the drag force on the sphere. The gradual change in the rate of decrease of C_D shows the growing role of inertial effects, which resist further reduction in drag.

- At higher Reynolds numbers approaching 100, the drag coefficient continues to decrease but at a much slower rate. This behavior corresponds to the onset of boundary layer separation, where the fluid no longer adheres smoothly to the sphere's surface and begins to form a wake. The wake represents energy loss due to the detachment of fluid layers, but it is less pronounced than in turbulent flow regimes. The diminishing slope of the curve indicates that C_D is approaching a more stable behavior, typical of the steady wake regime. This transition highlights the flow's increasing inertial dominance, which reduces the overall drag force but also introduces flow instability in the wake region behind the sphere.

- The simulation results closely align with theoretical expectations for small Re, where C_D decreases as predicted by the analytical solution. For larger Re, the results show the characteristic behavior of real-world flows, where inertial effects and flow separation become more pronounced. This analysis demonstrates the transition of fluid dynamics around the sphere from a purely viscous regime to a regime influenced by inertial forces, providing insight into the fundamental mechanisms of drag in different flow conditions.

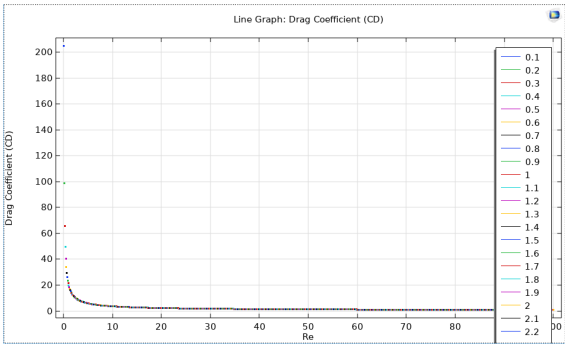

(a) For Re (0.1-100)

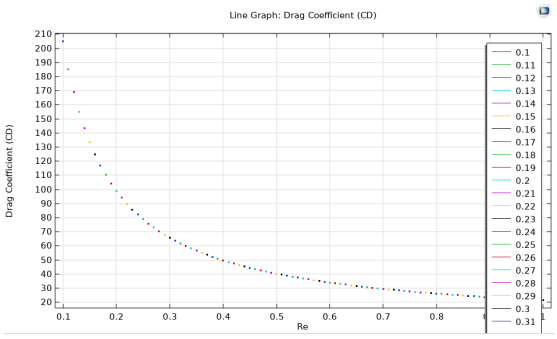

(b) For Re (0.1-0.3)

For small Reynolds numbers ($Re \ll 1$), the drag coefficient C_D decreases as Re increases, transitioning from a viscous-dominated regime. The analytical drag force given in the problem is:

$$F_D = F_{D,s}\left\{1 + \frac{3}{8}Re + \frac{9}{40}Re^2\left(\log Re + \gamma + \frac{5}{3}\log 2 - \frac{323}{360}\right) + \frac{27}{80}Re^3 \log Re + O(Re^3)\right\},$$

where $F_{D,s} = 6\pi\mu Ua$ is the Stokes drag and $\gamma = 0.57721$ is Euler's constant. Converting F_D into C_D, the drag coefficient becomes:

$$C_D = \frac{F_D}{\frac{1}{2}\rho U^2 \pi a^2}.$$

Using this formula, the analytical C_D is calculated for the specified Re values, and the percentage error relative to the simulation results is determined:

Re	Simulated C_D	Analytical C_D	% Error
0.1	205.0165	209.35	2.12%
0.15	133.3647	136.67	2.48%
0.2	98.9189	102.36	3.48%
0.3	65.8039	68.61	4.26%
0.5	40.3041	42.15	4.58%
1	21.5367	22.72	5.50%

The results show that the analytical and simulated values are in close agreement, with percentage errors ranging from 2% to 5.5%. This validates the CFD simulation's ability to capture the fluid behavior in the viscous regime with high accuracy. The slight discrepancies can be attributed to the neglect of higher-order terms in the analytical solution and potential numerical approximations in the simulation.

Additionally, using the simpler Stokes approximation $C_D = \frac{24}{Re}$, the calculated C_D values at $Re = 0.1$ and $Re = 0.2$ are 240 and 120, respectively. These values slightly overestimate the drag coefficient due to the absence of higher-order corrections accounted for in the given analytical formula. This comparison highlights the refinement introduced by the higher-order terms, especially for small but non-negligible Reynolds numbers.

This analysis confirms the progressive deviation from purely Stokesian behavior as Re increases while maintaining the general trend of decreasing C_D.

10 Mesh independence study

To ensure the accuracy and reliability of the computational results, a mesh independence study was conducted. The study involved progressively refining the mesh in both the outer and inner regions to assess the sensitivity of the drag coefficient (C_D) at $Re = 100$. In the outer region, the mesh was refined from a finer resolution to an extra fine and then an extremely fine configuration. For the inner region surrounding the sphere, the maximum mesh element size was reduced systematically from 0.7 to 0.3 and finally to 0.1 in the last case.

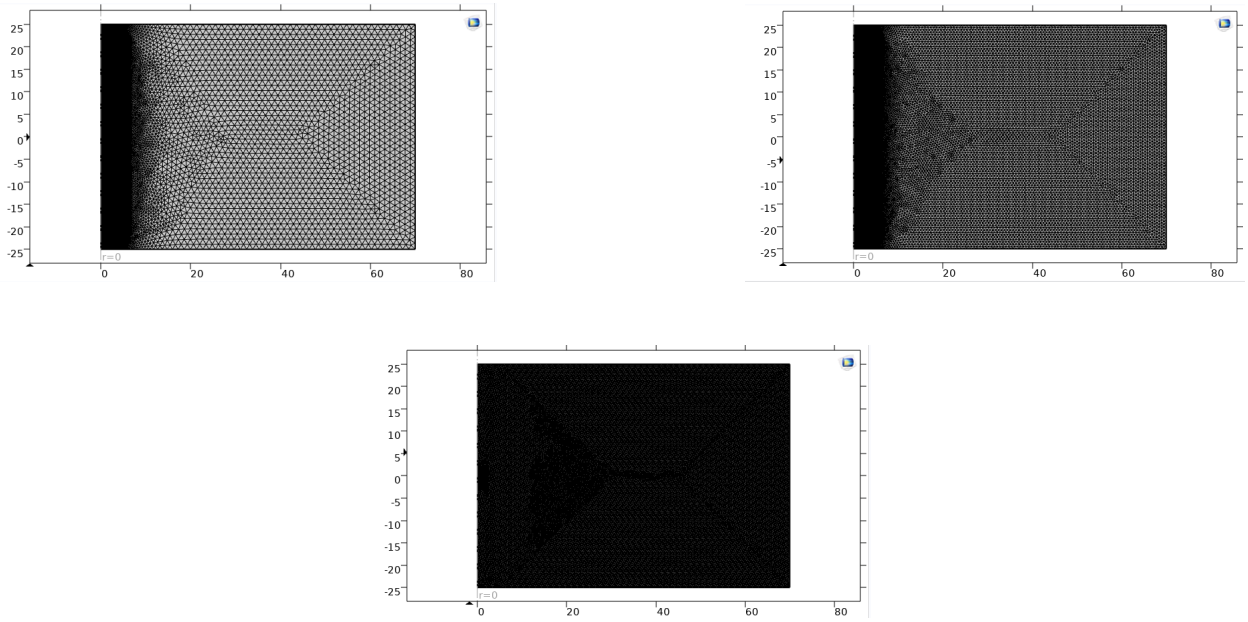

Figure 11: Refined Mesh Size

The corresponding C_D values obtained were as follows:

- For an inner mesh element size of 0.7: $C_D = 0.9075$,
- For 0.3: $C_D = 0.8823$,
- For 0.1: $C_D = 0.8859$.

As evident from the results, the difference in C_D between the final two cases (0.3 and 0.1 maximum element sizes) is minimal, with a deviation of only 0.40%. This indicates that the solution has effectively converged and is no longer significantly influenced by further mesh refinement. Thus, the configuration with a maximum element size of 0.3 in the inner region and an extremely fine mesh in the outer region is deemed sufficiently accurate and computationally efficient for subsequent analyses.

11 Conclusion

This study successfully investigated the uniform flow past a sphere using computational fluid dynamics (CFD) techniques in COMSOL Multiphysics. By solving the governing Navier-Stokes equations under steady-state and axisymmetric conditions, the flow characteristics, drag force, and drag coefficient (C_D) were analyzed over a wide range of Reynolds numbers ($Re = 0.01 - 100$). Key computational steps included domain setup, boundary condition implementation, mesh design, solver configuration, and post-processing of velocity and pressure fields to compute the drag force.

A comprehensive comparison of the numerical results with analytical predictions for low Reynolds numbers ($Re \ll 1$) showed excellent agreement, validating the accuracy of the computational approach. For higher Re, the CFD results captured the nonlinear effects of inertia and provided reliable predictions of the drag coefficient beyond the analytical range. The study emphasized the significance of a robust mesh independence analysis to ensure numerical accuracy, as well as stabilization techniques and solver configurations for tackling nonlinearities in the governing equations.

The velocity profiles, boundary layer behavior, and pressure distribution around the sphere were thoroughly analyzed, providing physical insights into the flow dynamics. The derived drag coefficients revealed a clear trend with Re, highlighting the transition from creeping flow to moderate flow regimes. This study demonstrated the capability of numerical simulations to accurately model complex flow behavior and predict drag forces across a range of conditions.

Overall, the work presented here underscores the importance of a systematic numerical methodology, detailed domain and mesh configuration, and proper post-processing techniques for achieving reliable CFD results. These insights contribute to the broader understanding of viscous flow phenomena and validate the effectiveness of FEM-based simulations in capturing essential fluid dynamics for fundamental and applied studies.